Modelling real particle shape in DEM: a comparison of two methods with application to railway ballast

Mathias Tolomeo [*], Glenn R. McDowell

Nottingham Centre for Geomechanics, University of Nottingham, Nottingham, NG7 2RD, United Kingdom

A B S T R A C T

Two different methods for the modelling of real particle shape in 3D DEM simulations are assessed in this paper. The first method uses overlapping spheres (clumps), while the second uses a block defined as a closed and convex polyhedron. The two methods are applied to the modelling of triaxial tests on a railway ballast. The macroscopic responses obtained with the two methods are compared, and it is observed that with clumps a higher shear strength, closer to the experimental response, can generally be achieved. A micromechanical analysis is also carried out to highlight how the modelled particle shape affects the mechanics, and consequently explain the difference in the macroscopic response. It is observed, in particular, that a key feature of real particle shape is concavity, that plays an important role in the mechanics of a granular assembly. Finally, the combined effect of particle shape and interparticle friction coefficient on the shear strength is assessed. This confirms that even for real (angular) shapes, peak strength increases with interparticle friction, while critical state strength first increases and then tends to saturate above a certain interparticle friction.

1. Introduction

While the mechanical behaviour of a granular material is affected by a large number of factors, it is well known that particle shape plays a fundamental role. Most granular materials that are of interest in the context of soil mechanics are composed of grains with irregular shapes, that may differ from a sphere. This directly affects the mechanics of the granular assembly, as grains with irregular shapes are generally more prone to interlocking and can build more stable configurations, which in turn leads to a higher shear resistance.

Historically, the Discrete Element Method (DEM) has been extensively employed to numerically model the mechanical behaviour of granular materials making use of simple shapes (spheres or disks), sometimes implementing other ingredients such as rolling resistance to simulate the additional resistance to particle rotation due to irregular geometries. In the last two decades, the improvements in imaging and digitalisation techniques have made it possible to acquire real particle morphology to a very high degree of accuracy. Meanwhile, the increase in computational power has allowed for the development of several techniques to model such irregular shapes in DEM simulations. Different methods are useful depending on the physical phenomenon under investigation. In this paper, two of the most popular methods available

in DEM commercial codes are considered, and their efficacy at modelling the mechanical response is assessed and compared. The first method models the irregular shape by means of a set of overlapping spheres of different sizes, behaving as a rigid body (apart from at surface contacts) as its internal contacts are neglected. Such an arrangement of spheres is usually referred to as a "clump". Clumps have the benefit of a simple treatment of contacts between bodies, as such contacts are basic interactions between spheres; however, this method can become computationally expensive as the number of spheres, and therefore the accuracy of the irregular shape representation, increases. The second method considered here makes use of convex polyhedra that can be simply defined by a closed triangular mesh enclosing a volume.

In the following sections, the principles of the two methods will be summarised; then, the two methods will be used to model a specimen of railway ballast subject to triaxial compression, and the mechanical response in the two cases will be compared. A micromechanical analysis will then be performed to relate the macroscopic response to local quantities that can describe the influence of particle shape. Finally, some results will be presented on the effect of a change in the interparticle friction angle on the mechanical response for an assembly of real-shaped particles.

---

* Corresponding author.
  E-mail address: mathias.tolomeo@nottingham.ac.uk (M. Tolomeo).

2. Real particle shape modelling in DEM

The advances in imaging techniques such as 3D laser scanning and X-Ray Computed Tomography (XRCT) made it possible to acquire ever richer information on the shape of real particles, especially for those composing coarse-grained soils such as sand and gravel[1–3].

Exploiting the long history of DEM simulations employing spheres (and equivalently disks in 2D), the first attempts to capture the geometry of the grain followed the same path, *i.e.*, using collections of spheres to fill the volume of an irregularly shaped particle[4–8].

Another popular way of modelling particle shape in 3D uses convex polyhedra, defined by a closed triangulated mesh describing the grain surface that can be easily derived from the most common digitalisation techniques.

When modelling railway ballast, particle shape plays a particularly important role, both because of the angular nature of the clasts composing a typical ballast, and because the usual laboratory experiments (*e.g.*, large triaxial compression and direct shear tests) generally involve a rather low number of single grains, in the order of 10^3, which from a computational point of view makes it easier to focus on modelling irregular shapes than it would be with, *e.g.*, sand specimens where the number of grains can be at least 1–2 orders higher. Therefore, both these methods have seen an extensive application to the case of ballast; examples include, among others, [9–13] for clumps, and [14–16] for convex polyhedra. Because of this, and considering the popularity of the two methods in general DEM applications, as well as their implementation in the most popular DEM codes (e.g. PFC3D), it was decided to focus on these two modelling schemes and assess their mechanical performances.

Alternative methods to the modelling of real shapes also include the use of hybrid shapes such as sphero-polyhedral clumps used in [17], the explicit modelling of the exact particle surface, such as the use of level set (LS) imaging that mathematically represents the surface of each grain as obtained from XRCT[1,18,19], or Fourier descriptors to replicate the geometry of 2D grains[20].

When assessing the fidelity of a shape modelling method to the corresponding real shape, it is essential to define relevant metrics for the quantification of shape. In the next section, the method adopted to this purpose is briefly presented, followed by a detailed description of the two methodologies considered for shape modelling, *i.e.*, clumps and convex polyhedra.

2.1. Shape quantification

The analysis of particle morphology is conventionally divided into three levels, describing the scales at which shape irregularity can be characterised: these are typically referred to as *form*, *angularity* and *roughness*. In this work it was decided to assess the fidelity of particle reconstruction only based on form, discarding the other two levels, as angularity still lacks a clear and unique definition, and cannot be easily determined for clumps where the identification of corners could be problematic, whereas roughness is directly accounted for through the contact law (interparticle friction angle). Form was quantified based on the recent work of Orosz et al.[21]. This method avoids the arbitrary definition of a basic, equivalent shape (*e.g.*, a bounding box or a best-fit ellipsoid), and at the same time exploits the richness of information coming from the description of the whole surface of the particle. Given a 3D polygonal mesh enclosing the particle's volume, a Surface Orientation Tensor (SOT) is defined for a single particle as a weighted fabric tensor obtained from the normal vectors at each of the mesh facets: $f_{ij} = \frac{1}{A}\sum_k n_i^k n_j^k A^k$, where $\overrightarrow{n}^k$ is the normal vector to the facet of area A^k, and $A = \sum_k A^k$ is the total surface area. Form metrics are then defined based on the three eigenvalues of this tensor ($f_1 \geq f_2 \geq f_3$), namely the compactness index $C = \frac{f_3}{f_1}$, flatness $F = \frac{f_1 - f_2}{f_1}$ and elongation $E = \frac{f_2 - f_3}{f_1}$. These metrics proved capable of capturing the features of irregular morphologies while keeping the objectivity of their definition and were therefore adopted in this work to quantify form of all the shapes considered, *i.e.*, the particle surface description obtained from 3D laser scan, and the clumps and polyhedra used to model it in DEM.

2.2. Clumps

The main advantage of using clumps to model real particle shape is that all interactions between bodies are reduced to simple sphere to sphere contacts, which can be very easily and efficiently resolved. However, the ability of a clump to simulate the mechanical effect of irregular shape will depend on the accuracy of the geometrical description, which is a function of the number and size of spheres used to build the clump. This, in turn, affects the computational effort that is required. A compromise should be sought between these two aspects. While in general a relatively low number (~10–20) of spheres has proven capable of capturing at least the first order of particle shape (*i.e.*, form), it is generally not sufficient to reproduce the sharp corners that characterise angular grains; moreover, unless a very high number of spheres is used (> 200), clumps will tend to show an unnatural "bumpiness" of their surface, which does not reflect the reality.

In this work, the generation of a clump to replicate an irregularly shaped body follows the method proposed by [22] and integrated in the commercial software PFC3D[23]. The algorithm takes as input a closed surface *S* defined by a triangular mesh and fills it with spheres. Two parameters control this operation: the size of the smallest sphere, defined as the ratio ρ to the size of the largest sphere that can be fitted; the proximity of two spheres, described by the angle θ between the two tangent vectors at the intersection between two spheres (Fig. 1). This angle is a measure of how much two spheres can overlap, ranging between $0°$ (no overlap) and $180°$ (complete overlap). The first parameter is particularly important for very angular shapes, as it acts on the sharpness of corners, while the second parameter controls the smoothness (and, in contrast, the "bumpiness") of the surface; both parameters affect the total number of spheres. An example of a clump is shown in Fig. 2.

The influence of such parameters on shape was assessed by computing shape metrics as presented in Section 2.1. While the definition of such metrics naturally applies to particle scans and polyhedral shapes, both of which are already defined by a 3D triangular enclosing mesh, the surface definition of clumps needed to be discretised in a similar way, with its smoothness depending on the resolution (number of faces/nodes) adopted. A similar resolution as in the particle scans ($\sim 10^4 - 10^5$ faces) was found to give a sufficiently smooth approximation of a clump's surface.

The shape analysis is performed on a dataset of 50 clumps obtained from a single particle shape – a triangular mesh with 38000 nodes and 76000 faces captured from a 3D laser scan of one granite ballast grain – using a range of values for the two parameters ρ and θ. Fig. 3 shows the compactness, flatness and elongation as defined from the Surface Orientation Tensor; unsurprisingly, these parameters approach the value of the reference mesh as the resolution of the clump and the number of spheres increase, *i.e.*, for decreasing ρ and increasing θ.

In previous applications of the clump technique to model angular grains such as the clasts composing railway ballast, the number of spheres used has increased as technological advancements allowed for higher computational power, starting with 10–20 (*e.g.*, [9,11]) and then rising up to 30–40 [12], 60 [13] and eventually 200 [10]. The DEM simulations presented in this paper make use of clumps obtained with $\rho = 0.3$ and $\theta = 140°$ (as in Fig. 2), with an average of 60 spheres each, which was found to be a good trade-off between computational efficiency and shape accuracy[13], with form descriptors very similar to the grain's, although at the cost of some corner sharpness and surface smoothness. A detailed study on the effect of these two parameters – and, more generally, of clump resolution – on the mechanical and volumetric behaviour of a specimen is out of the scope of this work, although it will
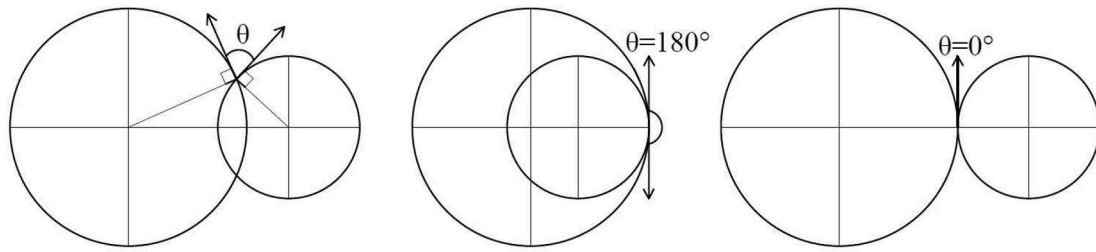
Fig. 1. Illustration of ball proximity defined by the angle θ. Left: generic case with $0° < \theta < 180°$; centre and right: smoothest and roughest case, with $\theta = 180°$ and $\theta = 0°$ respectively.
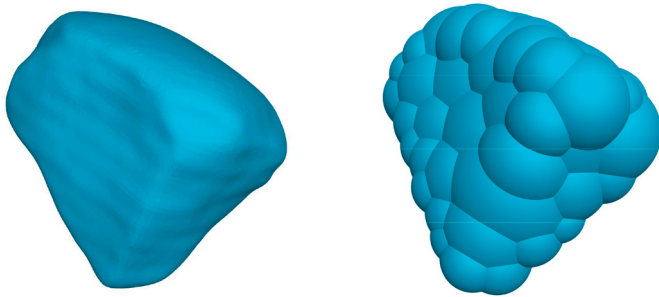

Fig. 2. Left: a triangular mesh made of 76000 faces from a 3D laser scan of a granite ballast grain. Right: a clump made of 56 spheres, obtained from the mesh on the left, having set $\rho = 0.3$ and $\theta = 140°$.

be worth exploring in the future.

2.3. Polyhedra

Polyhedra can also be used in the software PFC3D to model complex morphologies, provided that a closed, convex and manifold triangular mesh is used to define the particle's surface. Where the reference mesh is concave, its convex hull, *i.e.*, the smallest convex volume that contains it, is computed and used instead. Convexity is required because the typical algorithms of contact detection work with convex shapes; for concave shapes, a complicated decomposition of the object into many non-convex objects would be necessary, making this approach impractical. The influence of this morphologic constraint on the mechanical

behaviour will be discussed in Sections 4.1-4.2. From a computational point of view, convex polyhedra have the advantage of requiring the treatment of fewer interactions than would be the case with an analogous clump assembly, because, for the same number of polyhedra and clumps, the pairs of bodies to which the contact detection algorithm is applied is significantly smaller for the former compared to all the pairs of spheres making up clumps; moreover, the number of actual contacts itself is also generally lower, since contact between two convex bodies can only occur at one point, while pairs of clumps generally have multiple contact points, due both to their natural concavity and to the bumpiness of their surface. On the other hand, the contact detection algorithm itself is in general more cumbersome than it is for basic sphere interactions, due to the determination of the overlapping volume between the two irregularly shaped bodies, and it can become expensive as the number of faces grows. A comparison of the computational efficiency of the two strategies is not straightforward, as the two effects tend to balance out, and out of the scope for this work, which focuses on the effect on the mechanical response.

To limit the computational effort when using polyhedra, the reference particle mesh used in this work, made of $10^4 - 10^5$ faces, is first subjected to a simplification process through the quadric edge collapse decimation algorithm, that reduces the number of faces[24]. To analyse the effect of this procedure on shape, several levels of simplification have been considered for one unit-volume reference shape, from extremely simplified meshes made of few tens of faces to few thousands. Then, the convex hull was computed for each of these simplified meshes. Fig. 4 and Fig. 5 show respectively, for these convex shapes, the volume and the form descriptors (compactness, flatness and elongation computed from the Surface Orientation Tensor) as a function of the
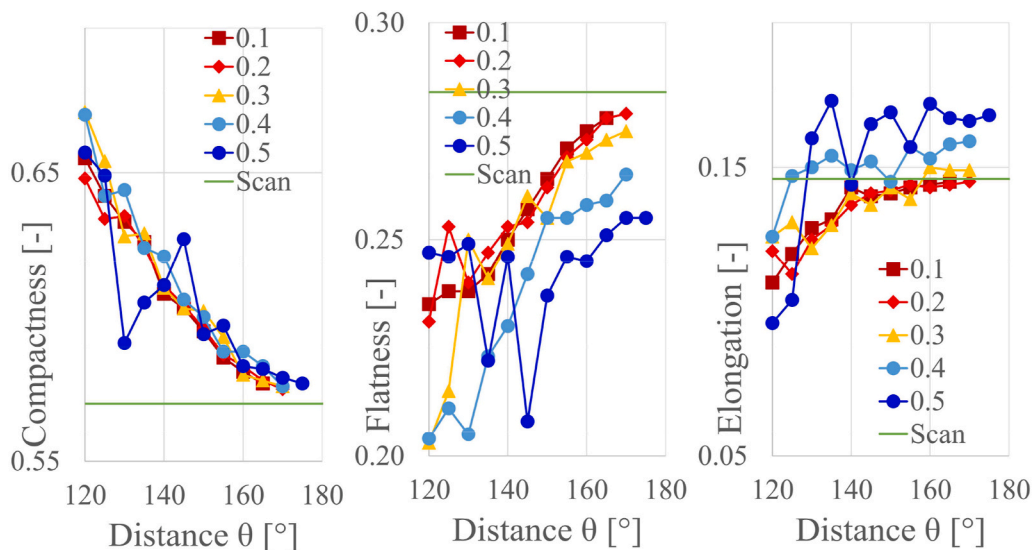

Fig. 3. Shape descriptors (left: compactness; centre: flatness; right: elongation) based on the Surface Orientation Tensor for clumps with different ρ (each corresponding to a different line) and θ. The dashed lines show the reference values for the original mesh.
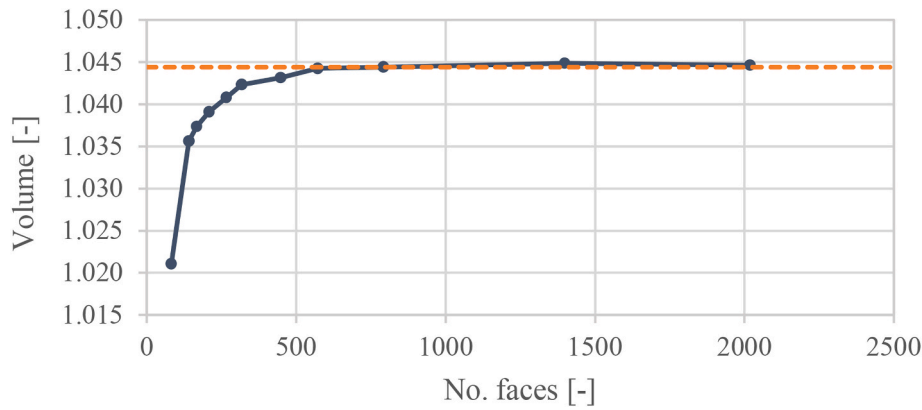
Fig. 4. Volume of polyhedra obtained as convex hulls of unit-volume meshes with different levels of resolution for one particle morphology. The dashed line represents the volume of the convex hull of the reference (full resolution) mesh.
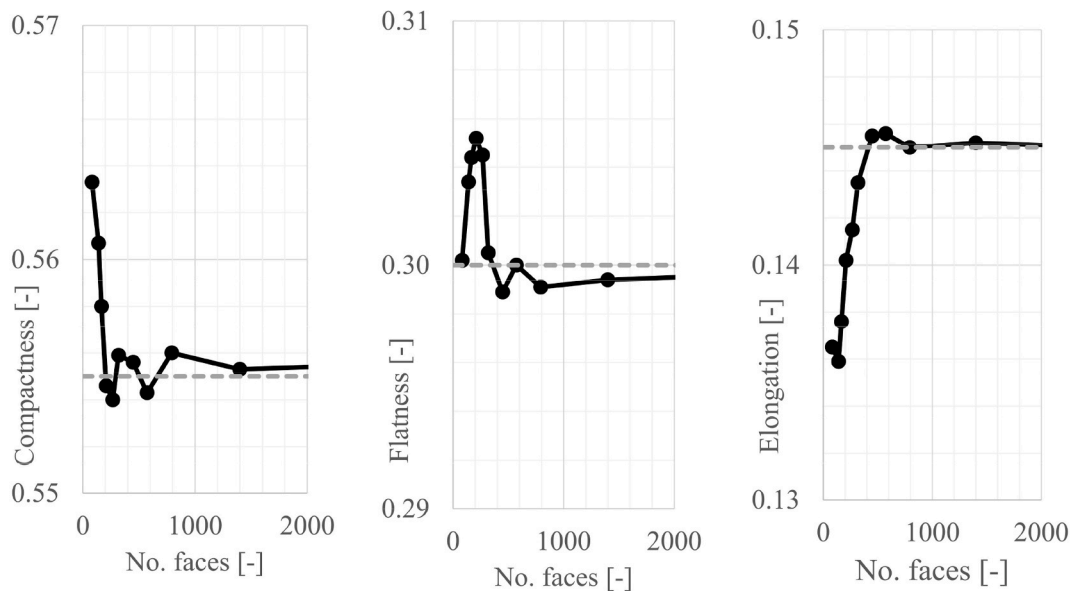

Fig. 5. Shape descriptors (left: compactness; centre: flatness; right: elongation) based on the Surface Orientation Tensor for polyhedra obtained as convex hulls of unit-volume meshes with different levels of resolution for one particle morphology. The dashed line represents the values for the convex hull of the reference (full resolution) mesh.

number of faces. All these quantities tend to diverge from the reference value (the convex hull of the non-simplified mesh) for low number of faces (few tens to few hundreds), while for convex hulls with more than 400–500 faces all metrics seem to converge, showing that a further increase in resolution of the convex hull beyond these values does not alter the main morphologic features. Therefore, all simulations presented in this work will make use of convex polyhedra with an average of about 450 faces each; the computational cost was comparable to that for 60-spheres clumps.

3. Simulation of a large triaxial test on railway ballast

DEM simulations were performed to reproduce a typical experimental test on railway ballast carried out in the large triaxial device in use at the University of Nottingham[25]. This machine allows testing of cylindrical ballast specimens with a diameter of 300 *mm* and a height of 450 *mm*. The specimen is enclosed laterally by a flexible natural rubber membrane with 4 *mm* thickness, and vertically by two stainless steel platens; after confinement is carried out, vertical loading is applied by moving upwards the lower ram and platen. Sample preparation in these tests follows a standard, three-steps vibro-compaction procedure that

has proven to consistently give an initial voids ratio close to 0.700 with respect to the initial volume of the cylindrical sample (corresponding to a total mass of about 49 *kg*). The particle size distribution (PSD) follows the British Standards for railway ballast gradation[26].

In the simulations, the same voids ratio was targeted, although the preparation procedure was not replicated; particles were instead generated with random positions and orientations inside the cylindrical volume, following a size distribution scaled down from the target PSD, and then slowly expanded until the target voids ratio was reached. This process was kept sufficiently slow so that the final sample would be stress-free. The PSD of the prepared sample is shown in Fig. 6. Particle shape was modelled with reference to a library of three different morphologies captured via 3D laser scans and shown in Fig. 7; shape metrics for such particles are reported in Table 1. A total of 747 particles were generated, which were uniformly distributed in the three different shapes.

To allow for a consistent comparison in terms of shape modelling strategies between clumps and polyhedra, two perfectly equivalent samples were created with the two methods. The first sample uses clumps with an average of about 60 spheres (with parameters $\rho = 0.3$ and $\theta = 140°$). Once this was prepared following the previously
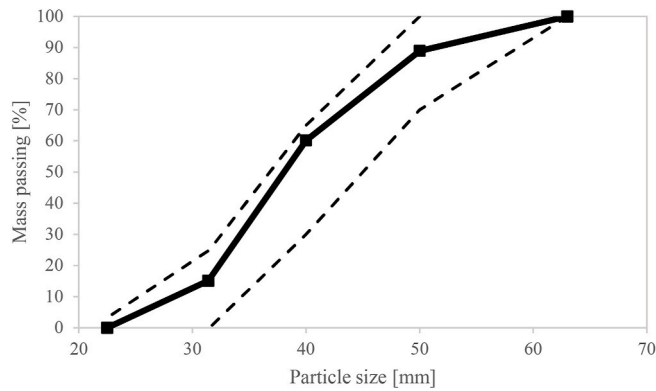
Fig. 6. Particle size distribution for the numerical specimen (solid line) and limits defined by the British Standards (dashed lines).
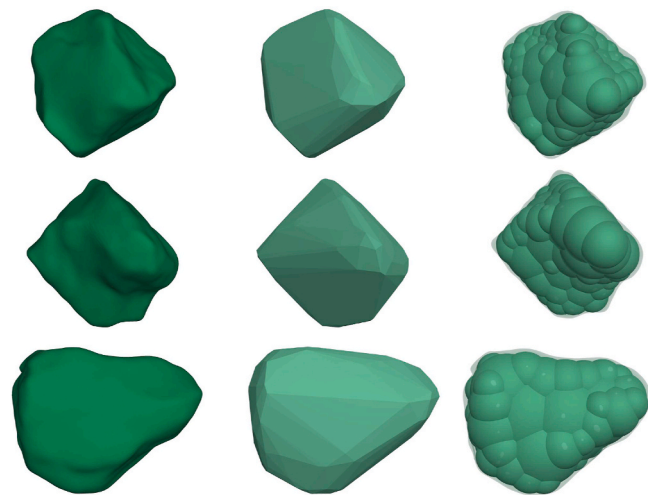

Fig. 7. The three shapes used to build the sample: original mesh (left), corresponding polyhedron with 450 faces (centre) and clump with 60 spheres (right).

described procedure, a second sample was created by replacing each clump with a polyhedron obtained from the same original shape, with the same position, orientation and volume as the parent clump (Fig. 8).

A simple linear contact law in the normal direction, and linear elasto-plastic with Coulomb friction in the tangential direction, were used to model contact interactions, assuming for ballast grains an arbitrary normal and tangential stiffness $k_n = k_s = 3 \cdot 10^6 N/m$. A relatively high interparticle friction coefficient $\mu = 0.8$ was chosen, which is not unusual for ballast simulations[12,14]. During confinement, however, a lower friction coefficient ($\mu = 0.3$) was used, in order to have a slightly denser and better coordinated (more contacts) sample and compensate for the sample preparation technique, which, compared with the experimental procedure, had no phase of vibratory compaction. A density of 2650 kg/m^3 – a typical value for granite – was assigned to ballast clasts. Given the quasi-static nature of the problem, it was safe to employ Cundall's local

damping[23] to help the system reach equilibrium; a (inertial) damping coefficient $\alpha = 0.7$ was adopted. In all these simulations gravity was not included. The main model parameters are summarised in Table 2.

The two end platens were modelled by (fixed) disks (no rotation), that were assigned the same stiffness properties as the ballast grains, and were assumed to be frictionless, which is a fair assumption considering that the end platens are carefully lubricated using sheets of greased latex before testing.

3.1. Flexible membrane

Modelling a flexible membrane in DEM simulations of triaxial tests can be crucial for the correct application of a uniform lateral pressure and for an accurate estimation of volumetric deformations. This is especially important when simulating ballast, since the relatively large size and small number of clasts cause a particularly irregular profile of the membrane, far from the assumption of right-cylinder deformation, with the shape of single clasts clearly emerging from underneath the membrane as this gets wrapped around the sample and folded into gaps between clasts. Several attempts have been made in the past to model a flexible membrane in 3D DEM, mostly including – but not limited to, see *e.g.* [27,28] – the use of a layer of bonded monodisperse spheres[1,13,29,30]. A
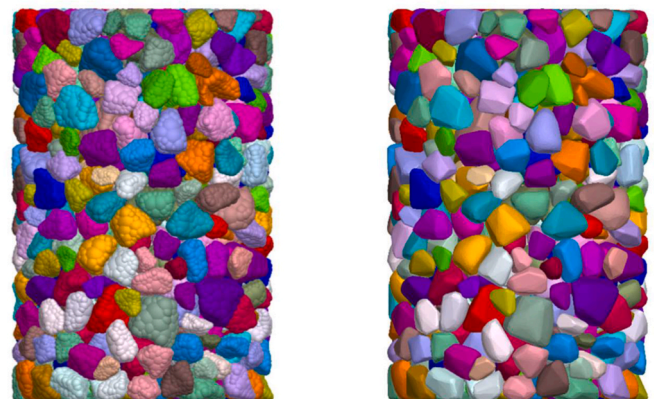

Fig. 8. Image of the two triaxial samples made of 747 grains, respectively modelled with clumps (left) and polyhedra (right). The same random colourisation was used for the grains in the two images.

Table 2
Main model parameters.

Number of particles	747
Initial sample dimensions (height x diameter)	$450 \times 300\ mm$
Interparticle friction coefficient – confinement	0.3
Interparticle friction coefficient – shearing	0.8
Platen friction coefficient	0
Normal contact stiffness – ballast grains	$3 \cdot 10^6\ N/m$
Tangential contact stiffness – ballast grains	$3 \cdot 10^6\ N/m$
Normal contact stiffness – platen	$3 \cdot 10^6\ N/m$
Confining pressure	$60\ kPa$
Particle density	$2650\ kg/m^3$
Damping coefficient	0.7

Table 1
Shape properties for the three particle morphologies used in the DEM large triaxial simulations and for the corresponding clumps ($\rho = 0.3$ and $\theta = 140°$) and polyhedra.

	Compactness			Flatness			Elongation		
	Scan	Clump	Poly	Scan	Clump	Poly	Scan	Clump	Poly
Shape 1	0.521	0.568	0.518	0.398	0.347	0.396	0.080	0.084	0.086
Shape 2	0.541	0.577	0.526	0.365	0.329	0.366	0.095	0.093	0.108
Shape 3	0.520	0.560	0.517	0.205	0.203	0.212	0.275	0.237	0.271

similar approach is also adopted in this work; the main properties are summarised in Table 3. Fig. 9 shows this membrane in the undeformed configuration and after isotropic confinement, where the irregular profile is clearly visible. In the initial configuration, spheres have a little overlap with their neighbours, to help avoid gaps; a lower density than that for natural rubber is therefore assigned to each sphere, to compensate this effect as well as the excess thickness, so that the total mass matches the membrane mass.

4. Macroscopic response and micromechanical analysis

After grain generation and expansion, the sample (at $e_0 = 0.700$) was confined by gradually increasing the applied pressure up to the target value of 60 kPa. As previously mentioned, during this phase only a lower interparticle friction coefficient ($\mu = 0.3$) was used, in order to achieve a better coordination. After equilibrium was reached, friction was set to the final value of 0.8 and the two samples were sheared through the application of a constant velocity $v = 10^{-3} m/s$ to the lower platen, until an axial strain of 30% was reached. This velocity is larger than the velocity generally used in experiments, which, if used here, would cause simulations to be impractically long. To verify the assumption of the problem being quasi-static, so that inertial effects could be neglected, the inertial number $I = \dot{\varepsilon}\sqrt{\frac{m}{pd^{D-2}}}$ was calculated, where $\dot{\varepsilon}$ is the strain rate applied, m is the typical mass of a grain, p the mean pressure, d the average grain diameter and D the dimension of the system. With the chosen platen velocity, a value of $I < 10^{-3}$ was obtained, satisfying the condition of quasi-staticity[31].

The mean stress in the assembly is computed directly from the contact forces, as is common practice in DEM, following the expression $\sigma_{ij} = \frac{1}{V}\sum_{N_c}f_i l_j$[32], where contact quantities $\overrightarrow{f}$ (contact force) and $\overrightarrow{l}$ (branch vector connecting the centroids of the two bodies in contact) are summed over all contacts N_c lying inside volume V. The evolution of the mobilised friction angle $\varphi = \sin^{-1}\left(\frac{\sigma_1 - \sigma_3}{\sigma_1 + \sigma_3}\right)$, where σ_1 and σ_3 are the major and minor principal stresses respectively, is shown for the two simulations and for an equivalent laboratory experiment in Fig. 10. Polyhedra show a sensibly softer behaviour in the early stages of deformation and a generally smaller strength throughout the whole test, while clumps allow for a closer fit with the experimental curve (which is however limited to an axial strain $\varepsilon_a = 12\%$ due to constraint imposed by the volume measurement system). A peak friction angle $\varphi_{peak} = 43.8°$ is reached by the sample made of clumps, while with polyhedra the peak angle is lower (41.3°). At critical state, the two curves tend to approach a common value close to 30°.

Having managed to isolate particle shape from all the other factors that may affect the mechanical response, it is possible to speculate on the nature of this difference with reference only to morphology. However, this difference cannot be easily explained by only looking at the classic shape metrics: as shown in Table 1, the metrics which describes the *form* of the particle are similar between clumps and polyhedra, and in both cases they reflect well the modelled morphology. Since shape metrics alone seem not sufficient, it was decided to carry out a micromechanical analysis to find a clearer connection between shape and the local
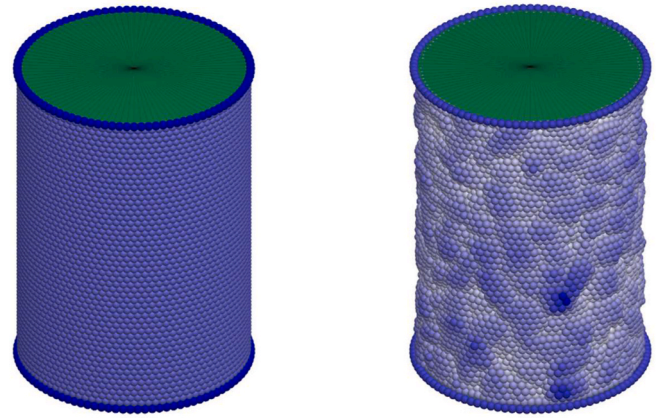
Table 3
Main parameters of the flexible membrane.

Number of spheres	5600
Membrane dimensions (height x internal diameter)	450×300 mm
Membrane sphere linear bond model – membrane normal stiffness	$2 \cdot 10^3$ N/m
Membrane sphere-ballast linear model – membrane normal stiffness	$10^6 N/m$
Sphere-grain friction coefficient	0
Membrane sphere density	385 kg/m^3
Sphere radius	6.1 mm
Damping coefficient	0.7

Fig. 9. Layout of the membrane spheres in the undeformed configuration (left) and after isotropic confinement at 60 kPa (right). Spheres are colourised with respect to their distance from the sample initial axis.
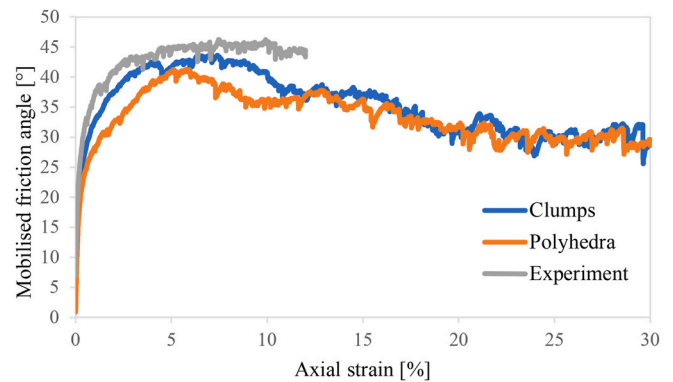

Fig. 10. Stress-strain response of triaxial tests on the two numerical samples and analogous experimental curve for a 60 kPa confining pressure.

mechanics, and therefore look for the origin of the macroscopic differences.

4.1. Concavity and multiple contacts in clumps

One crucial difference between the two shape modelling strategies is that polyhedra are convex by definition, while clumps, being simply agglomerates of spheres, can reproduce the concavity which naturally occurs in real ballast clasts. The concavity of clumps can in fact come from two distinct features, *i.e.*, the intrinsic concavity of the shape being modelled, and the gaps between neighbouring spheres which reflects the typical irregularity of clump surface, particularly when a low value of the parameter θ (and consequently of the number of spheres generated) is used when building the clump, as explained in Section 2.2. The effect that this has on the mechanics is in the number of possible interactions between two grains: while a contact between two convex polyhedra can only happen at a single point, with clumps several contact points between the same pair of grains can occur. In general, when there is more than one contact between two bodies, this gives a more stable configuration, because of the better ability of the grains to resist to rotations. However, not all multiple contacts between clumps have the same effect on the mechanics. In the same way as the concavity of clumps comes from two distinct sources, multiple contacts can also be associated with either of these sources; only those that occur because of the natural concavity of the particle shape are expected to have a substantial effect on the mechanics of the system. As for all those multiple contacts that are simply due to the bumpiness of the surface (resolution of the clump),

it can be assumed that they do not contribute much, *i.e.*, they could be replaced by a single contact force without much effect on the stress state of the particle.

A simple algorithm was defined to clearly separate multiple contacts in two groups based on this criterion. In the context of an interaction between two clumps, if this occurs at more than one contact point it means that multiple spheres are involved. If two spheres from the same clump are found to share a contact with the same sphere of the other clump, they are assumed to be "interconnected", and their contacts to be part of the same clump-clump interaction. By applying this criterion to all spheres involved in contacts between two clumps, groups of interconnected spheres and contacts can be defined. A group of such interconnected contacts can be seen as one unique mechanical interaction; such contacts will typically be relatively close to each other (with respect to some relevant dimension of the particle) and have similar normal orientations. If, on the other hand, no shared sphere can be found between two (groups of) contacts, that means those will form two distinct mechanical interactions. As confirmed visually (see examples in Fig. 11) and by metrics such as, *e.g.*, the distance between contact points or the orientation of the normal to the surface, this criterion proved successful at classifying contacts with respect to their contribution to the particle's mechanics. It should be noted that the examples in Fig. 11 refer to clumps built with a higher number of spheres, for which the visualisation of the distinct groups of contacts was easier; however, the algorithm has proven to work well also for clumps with a smaller number of spheres, as those used in the simulations presented here.

After identifying and grouping contacts in this way, it was possible to focus on separate groups of contacts and look at their contribution to the macroscopic stress response. The ratio of the number of contacts in each group, $N_c^{multiple}$ and N_c^{unique}, to the total number of contacts remained fairly constant throughout the whole test (about 60% of all contacts were identified as belonging to multiple interactions). Stress contributions of groups of contacts can be determined from contact quantities (force and branch vector) just like for the global average stress, taking only part of the contacts, so that two stress tensors are defined as follows: $\sigma_{ij}^{multiple} = \frac{1}{V} \sum_{N_c^{multiple}} f_i l_j$ and $\sigma_{ij}^{unique} = \frac{1}{V} \sum_{N_c^{unique}} f_i l_j$. For each stress contribution, the deviatoric part can be assessed, *e.g.*, through the mobilised friction angle φ. The evolution of φ for the two categories of contact is shown in Fig. 12, together with that for the whole assembly of clumps

and for the sample made of polyhedra (*i.e.*, the same two curves as in Fig. 10). The contribution of contacts that belong to multiple grain-grain interactions shows a substantially higher shear strength than that of contacts that belong to single interactions, confirming that clumps allow for more stable configurations, where grains are globally more resistant to rotations. This difference becomes more evident as the applied strain increases; it is still small or negligible when strains are low (below 2%) and little rearrangement of grains has occurred. The contribution of unique contacts between clumps is globally very similar to the overall strength of polyhedra, that can only have unique contacts due to their convexity. This suggests that the main difference between the two types of modelling shape, with respect to the mechanical behaviour, lies in the concavity of clumps and in their ability to build more stable local configurations.

4.2. Mechanics-based particle shape index

When the purpose of analysing shape is to look at its influence on the mechanics of the assembly, the common shape parameters can be replaced by alternative descriptors that are especially tailored to this purpose. Kawamoto et al.[19] have proposed an index which measures, for each point on the surface of a particle, the angle α between the contact normal (*i.e.*, the normal at the surface of the particle at that point) and the radial vector that connects the point with the particle's centre of mass. This parameter is closely related to the additional rotational resistance that a particle can offer due to its irregular shape, as can be seen in Fig. 13: while a sphere has $\alpha = 0°$, and the only rotational resistance comes from interparticle friction (unless artificially added in the contact law), real shaped particles can have $\alpha > 0°$, which means that even normal forces can generate a moment with respect to the centre of mass, and therefore they can potentially offer additional rotational resistance. By measuring α only at the contact points around a particle, one obtains a parameter (α_c) that is more suited to describe the effect of shape on the current mechanical state of the assembly.

In the context of the comparison between clumps and polyhedra, the role of concavity and asperities can be seen to influence also this aspect, as is schematically shown in Fig. 14 (for concavity), where a concave grain is compared with its convex hull (as can be used in the simulations with polyhedra). When generating a convex hull, depressed regions typical of concave shapes get flattened, and this has the effect of rotating the normal at the surface in a way that its angle α with the radial vector becomes smaller than it would be if the concavity was preserved.

This is confirmed by the statistical distribution of α_c for all the contacts in an assembly, as shown in Fig. 15 for a state near the peak of the
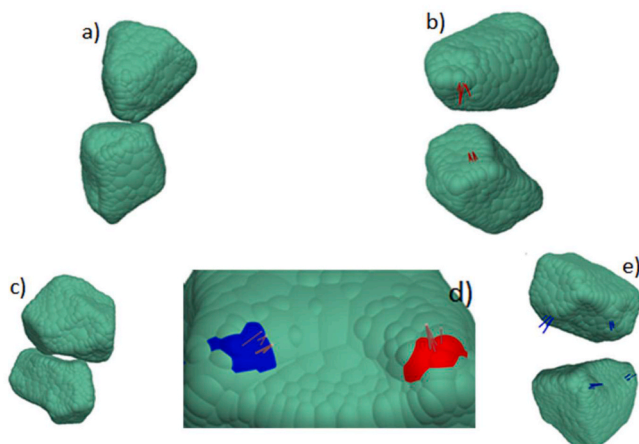
Fig. 11. Two examples (top row and bottom row) of application of the algorithm to identify and group multiple interactions between clumps. The same interaction is shown in two different views (grains in contact on the left; exploded view to show the contact locations on the right). a), b): a group of contacts that can be reduced to a single interaction. c), d), e): two groups of contacts can be identified here, defining two distinct interactions; d) is a close-up view of one of the two clumps with clear indication of the spheres engaged in contact.
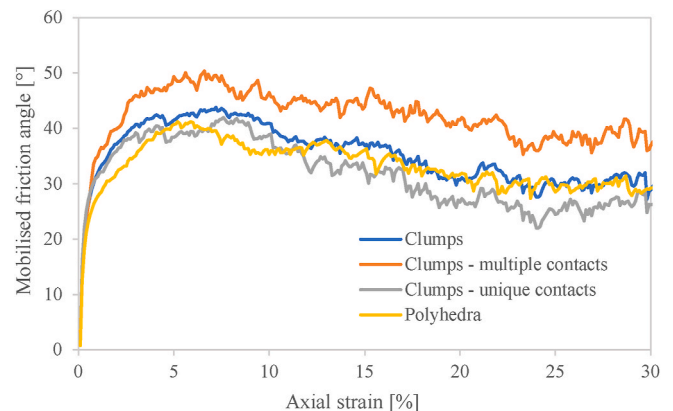
Fig. 12. Mobilised friction angle φ as a function of axial strain for clumps and polyhedra. For the simulation with clumps, φ is also shown for groups of contacts respectively belonging to multiple clump-clump interactions (*i.e.*, occurring at more than one point) and single interactions (occurring at one single point).
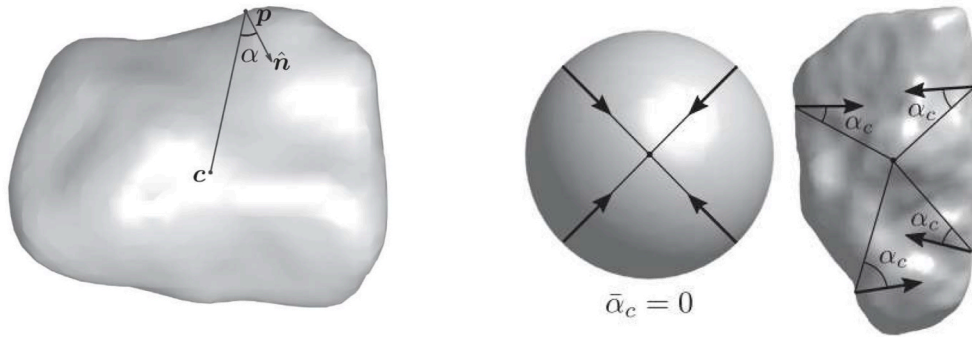
Fig. 13. Left: illustration of the shape parameter α, with $\vec{n}$ being the normal at the point p and $\vec{pc}$ the radial vector. Right: illustration of α_c at four contact points around a sphere and an irregular particle (no additional contribution to rotational resistance for a sphere with $\alpha_c = 0°$). Images from [19].
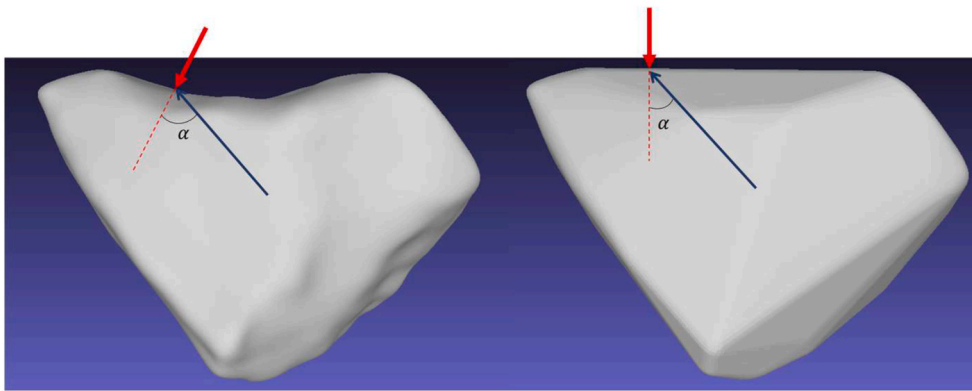

Fig. 14. Schematic illustration of the effect of concavity on the angle α (and therefore on the rotational resistance linked to shape). Left: 2D view of a scanned ballast grain, with indication of the normal to the surface at one point inside a concavity, the corresponding radial vector and the angle between them. Right: same illustration obtained for the convex hull of the shape on the left, giving a smaller α.

deviatoric stress for the two simulations shown before (though similar distributions were obtained also for an isotropically confined state). Contacts between clumps, due to their concavity, can form angles α_c even up to $80° - 90°$ which can offer a high rotational resistance, and more generally they show a higher probability of making angles above 40° than contacts between convex polyhedra. This also has an effect on the load transmission properties of the assembly. If contacts are grouped, based on their α_c, into 10°-wide classes, then the stress tensor for each of these classes can be computed, in a similar way to what has been done in Section 4.1 for multiple and single contact interactions. For
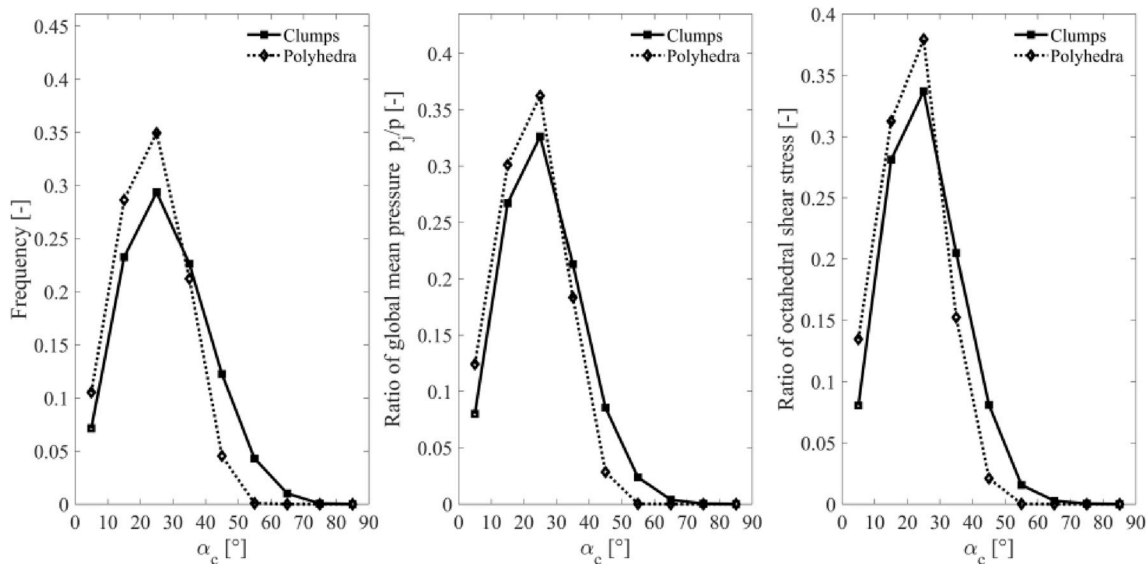

Fig. 15. Classification of contacts between grains near the peak of the curves in Fig. 10 ($\varepsilon_a = 7\%$) for two identical samples, made respectively of clumps and polyhedra. Left: probability distribution function (PDF) of angles α_c. Centre: ratio of mean pressure for each class of contacts (same intervals as in the PDF on the left) to the global mean pressure. Right: ratio of octahedral shear stress for each class of contacts to the global octahedral shear stress.

each class j with principal stresses σ_{1j}, σ_{2j}, σ_{3j}, mean pressure $p_j = (\sigma_{1j} + \sigma_{2j}, +\sigma_{3j})/3$ and octahedral shear stress $\tau_{oct,j} = \frac{1}{3}((\sigma_{1j} - \sigma_{2j})^2 + (\sigma_{2j} - \sigma_{3j})^2 + (\sigma_{1j} - \sigma_{3j})^2)^{1/2}$, the contribution to the global mean pressure $p = (\sigma_1 + \sigma_2 + \sigma_3)/3$ and global octahedral shear stress $\tau_{oct} = \frac{1}{3}((\sigma_1 - \sigma_2)^2 + (\sigma_2 - \sigma_3)^2 + (\sigma_1 - \sigma_3)^2)^{1/2}$ can be determined as $w_{pj} = \frac{p_j}{p}$ and $w_{\tau_{oct}j} = \frac{\tau_{oct,j}}{\tau_{oct}}$. Fig. 15 shows that, in an assembly of concave clumps, the contribution to load transmission in terms of both p and τ_{oct} for contacts with $\alpha_c > 30°$ is higher compared with an assembly of polyhedra, consistently with the higher number of such contacts. Therefore, a larger part of stress is carried by contacts which can offer a higher rotational resistance and thus can support a higher deviatoric stress, resulting globally in a higher macroscopic shear strength.

5. Combined effect of particle shape and interparticle friction

Together with particle shape, another ingredient that plays a crucial role in the shear strength of granular materials is interparticle friction. Since this is typically modelled through the simple Coulomb model, that only requires the definition of one single parameter – the interparticle friction angle Φ_{int} or the corresponding coefficient μ, defined as $\mu = \tan^{-1}\Phi_{int}$ – its influence on the peak and ultimate resistance has been widely studied in DEM, long before shape was taken into account. It is generally acknowledged that interparticle friction affects both peak and critical state strength. Some results, both from experiments on spheres[33,34] and DEM simulations on different basic particle morphologies (including disks[35,36], 2-disk clumps[37], polygons[38,39], spheres[40–42] and ellipsoids[43]), indicate that the peak strength monotonically increases with μ while the critical state angle tends to saturate for large μ. However, the effect of microscopic friction on real-shaped, angular particles has not been investigated yet.

The influence of μ was therefore studied in this work for two different samples, respectively made of clumps and polyhedra. The two samples were created by radial expansion of two sets of particles, similarly as in the procedure explained in Section 3; however, instead of reaching a target voids ratio $e_0 = 0.700$, grains were slowly expanded until they jammed, $i.e.$, they started developing persistent force chains. The densest stress-free configuration that was achieved in this way, immediately before jamming, was considered to be the densest state for that specific shape and PSD; this corresponded to an initial voids ratio (based on the volume of an undeformed cylinder) $e_0 = 0.490$ for clumps and $e_0 = 0.460$ for polyhedra. While particles underwent a further expansion and were therefore generally larger than the particles used in Section 3, the two PSDs still lied within the boundaries defined by the British Standards. These two samples were then confined under a $60\ kPa$ pressure with a very low friction angle ($\mu = 0.01$), so that both

assemblies were in their densest state at the end of confinement and the effect of sample density could be ruled out, as for both clumps and polyhedra the initial relative density could be assumed to be close to 100%. To investigate the effect of friction on the mechanical response, friction coefficient μ was then tuned only before the start of the shearing phase, with values between 0.1 and 0.7.

Fig. 16 shows the mobilised friction angle φ as a function of the local friction μ, for samples made of clumps and polyhedra. Shear strength was reported at different stages of the tests, namely at the onset of dilation (φ_d) – $i.e.$, when the initial contraction turns into dilation and $\frac{d\varepsilon_v}{d\varepsilon_a} = 0$ –, at peak (φ_{max}) and at critical state (φ_{cs}). The latter seems to confirm what observed in previous works: critical strength substantially increases between $\mu = 0.1$ and $\mu = 0.3$, but then remains almost unchanged for $\mu > 0.3$. The other two strength values, on the other hand, show a clearer correlation with μ, as they monotonically increase up to $\mu = 0.7$. Rowe[44] already showed that the shear strength at the onset of dilation can vary with local friction (and initial density), but assumed it could not be larger than φ_{cs}; Guo & Su[45] showed that for angular particles φ_d can be substantially higher than φ_{cs}, in line with what is observed here for $\mu \geq 0.3$. This can be explained in relation to the interlocking effect that, for angular particles, is more significant in the early stage of deformations, and then decreases as grains are forced to roll over each other, breaking the stable and "interlocked" initial configurations. The difference between peak and critical state strength also increases with μ, as does the maximum dilation rate $\left(-\frac{d\varepsilon_v}{d\varepsilon_a}\right)_{max}$; Fig. 17
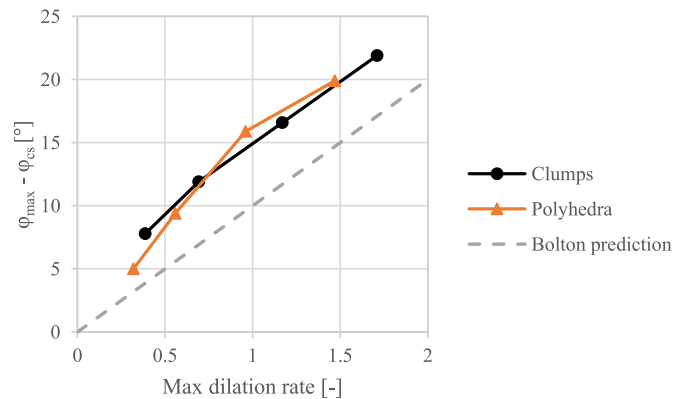

Fig. 17. Difference between the peak and critical state strength against the maximum dilation rate for clumps and polyhedra. In both cases a good fit with a linear relation, as postulated by Bolton[46], is observed. The dashed line shows the slope of Bolton's relation $\varphi_{max} - \varphi_{cs} = 10\left(-\frac{d\varepsilon_v}{d\varepsilon_a}\right)_{max}$.
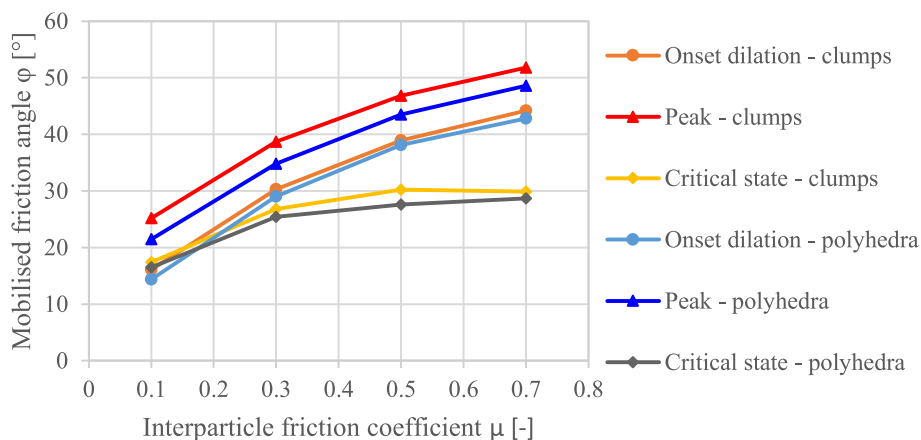

Fig. 16. Mobilised friction angle φ for clumps and polyhedra at different stages (onset of dilation, peak, critical state) and for different values of interparticle friction coefficient μ.

shows the relation between these two terms, which is in line with the linear correlation proposed by Bolton based on laboratory experiments on different types of sand[46].

6. Conclusions

In this paper, some aspects of the influence of particle shape on the mechanical response of a granular assembly were studied, with application to a particularly angular material such as railway ballast. Two of the most common modelling strategies that can be alternatively adopted to represent an irregular shape in DEM, and that are readily available in some of the most popular DEM codes, were analysed, namely clumps, *i. e.*, clusters of overlapping spheres with no internal contacts, and polyhedra. It was shown that, when constrained to be convex, the latter may systematically underestimate the shear strength as they do not reproduce concavity, which is found to play a crucial role in the mechanics of irregularly shaped granular materials. On one hand, concavity allows for multiple contact points between two bodies, which can lead to more stable configurations; on the other hand, it allows for contacts that can offer a larger rotational resistance, as measured by the angle between the contact normal and the radial vector connecting the contact point with the particle centre of mass. By isolating the part of the stress tensor due to concavity, the important role of concavity on mobilised friction was highlighted. This suggests that clumps, or other schemes capable of modelling concavity, should be preferred when choosing how to reproduce real shape features in coarse-grained soils.

The combined effect of shape and interparticle friction was also studied, with focus on how a change in the friction coefficient μ affects the mechanical response of an assembly of real-shaped angular particles. It was observed that the peak strength monotonically increases with interparticle friction, while the ultimate strength only increases for low values of μ and then tends to saturate for larger values. All these observations are in line with classic results for granular assemblies with basic morphologies (disks/spheres, polygons, ellipsoids).

While in this work the effect of real shape features on the mechanics of a granular material has been studied with a main focus on a first scale definition of shape, in the future also finer scale features should be considered, especially particle angularity and the effect of sharp corners on both the shear strength and the volumetric response. This could involve the use of higher resolution clumps, which preserve the simplicity of the contact resolution algorithm while offering a high accuracy in reproducing such morphologic features. While particle breakage can generally be excluded when low stress levels are considered, as in most applications on railway ballast, it might still be necessary to model some form of local damage when asperities and sharp corners are used, such as the chipping of asperities or a smoothening of the surface. These features, together with a better understanding of the mechanical behaviour at the contact between two grains, should complement a correct representation of particle shape with the purpose of accurately reproducing, and eventually replacing, some classic laboratory experiments with DEM simulations.

Declaration of competing interest

The authors declare that they have no known competing financial interests or personal relationships that could have appeared to influence the work reported in this paper.

Data availability

Data will be made available on request.

Acknowledgements

References

1 Kawamoto R, Andò E, Viggiani G, Andrade JE. All you need is shape: predicting shear banding in sand with LS-DEM. *J Mech Phys Solid*. 2018;111:375–392. https://doi.org/10.1016/j.jmps.2017.10.003.

2 Wiebicke M, Andò E, Herle I, Viggiani G. On the metrology of interparticle contacts in sand from x-ray tomography images. *Meas Sci Technol*. 2017;28(12). https://doi.org/10.1088/1361-6501/aa8dbf.

3 Le Pen L, Ahmed S, Zervos A, Harkness J, Powrie W. Resin recovery and the use of computed tomography for quantitative image analysis of railway ballast. *Civil-Comp Proc*. 2014;104:1–14. https://doi.org/10.4203/ccp.104.130.

4 Matsushima T, Katagiri J, Uesugi K, Tsuchiyama A, Nakano T. 3D shape characterization and image-based DEM simulation of the lunar soil simulant FJS-1. *J Aero Eng*. 2009;22(1):15–23. https://doi.org/10.1061/(ASCE)0893-1321(2009)22:1(15).

5 Garcia X, Latham J-P, Xiang J, Harrison JP. A clustered overlapping sphere algorithm to represent real particles in discrete element modelling. *Geotechnique*. 2009;59(9):779–784. https://doi.org/10.1680/geot.8.T.037.

6 Gao R, Du X, Zeng Y, Li Y, Yan J. A new method to simulate irregular particles by discrete element method. *J Rock Mech Geotech Eng*. 2012;4(3):276–281. https://doi.org/10.3724/sp.j.1235.2012.00276.

7 Ferellec JF, McDowell GR. A simple method to create complex particle shapes for DEM. *Geomechanics Geoengin*. 2008;3(3):211–216. https://doi.org/10.1080/17486020802253992.

8 Ferellec JF, McDowell GR. Modelling realistic shape and particle inertia in DEM. *Geotechnique*. 2010;60(3):227–232. https://doi.org/10.1680/geot.9.T.015.

9 McDowell GR, Li H. Discrete element modelling of scaled railway ballast under triaxial conditions. *Granul Matter*. 2016;18(3). https://doi.org/10.1007/s10035-016-0663-8.

10 de Bono J, Li H, McDowell GR. A new abrasive wear model for railway ballast. *Soils Found*. 2020;60(3):714–721. https://doi.org/10.1016/j.sandf.2020.05.001.

11 Indraratna B, Ngo NT, Rujikiatkamjorn C, Vinod JS. Behavior of fresh and fouled railway ballast subjected to direct shear testing: discrete element simulation. *Int J GeoMech*. 2014;14(1):34–44. https://doi.org/10.1061/(ASCE)GM.1943-5622.0000264.

12 Ngo NT, Indraratna B, Rujikiatkamjorn C. Micromechanics-based investigation of fouled ballast using large-scale triaxial tests and discrete element modeling. *J Geotech Geoenviron Eng*. 2017;143(2), 04016089. https://doi.org/10.1061/(asce)gt.1943-5606.0001587.

13 Zhang J, Wang X, Yin ZY, Liang Z. DEM modeling of large-scale triaxial test of rock clasts considering realistic particle shapes and flexible membrane boundary. *Eng Geol*. 2020;279(October), 105871. https://doi.org/10.1016/j.enggeo.2020.105871.

14 Deiros Quintanilla I, Voivret C, Combe G, Emeriault F. Quantifying degradation of railway ballast using numerical simulations of micro-deval test and in-situ conditions. *Procedia Eng*. 2016;143(Ictg):1016–1023. https://doi.org/10.1016/j.proeng.2016.06.096.

15 Harkness J. Potential particles for the modelling of interlocking media in three dimensions. *Int J Numer Methods Eng*. 2009;80(12):1573–1594. https://doi.org/10.1002/nme.2669.

16 Harkness J, Zervos A, Le Pen L, Aingaran S, Powrie W. Discrete element simulation of railway ballast: modelling cell pressure effects in triaxial tests. *Granul Matter*. 2016;18(3):65. https://doi.org/10.1007/s10035-016-0660-y.

17 Stasiak M, Combe G, Desrues J, Richefeu V, Villard P, Armand G. Experimental investigation of mode I fracture for brittle tube-shaped particles. *EPJ Web Conf Powders grains*. 2017:4–7. https://doi.org/10.1051/epjconf/201714007015, 07015.

18 Kawamoto R, Andò E, Viggiani G, Andrade JE. Level set discrete element method for three-dimensional computations with triaxial case study. *J Mech Phys Solid*. 2016;91:1–13. https://doi.org/10.1016/j.jmps.2016.02.021.

19 Kawamoto R, Andrade JE, Matsushima T. A 3-D mechanics-based particle shape index for granular materials. *Mech Res Commun*. 2018;92:67–73. https://doi.org/10.1016/j.mechrescom.2018.07.002.

20 Mollon G, Quacquarelli A, Andò E, Viggiani G. Can friction replace roughness in the numerical simulation of granular materials? *Granul Matter*. 2020;22(2):1–16. https://doi.org/10.1007/s10035-020-1004-5.

21 Orosz Á, Angelidakis V, Bagi K. Surface orientation tensor to predict preferred contact orientation and characterise the form of individual particles. *Powder Technol*. 2021;394:312–325. https://doi.org/10.1016/j.powtec.2021.08.054.

22 Taghavi R. Automatic clump generation based on mid-surface. In: *The 2nd International FLAC/DEM Symposium*. 2011:791–797.

23 PFC — Particle flow code, Vertex. 7.0. 2021.

24 Cignoni P, Callieri M, Corsini M, Dellepiane M, Ganovelli F, Ranzuglia G. MeshLab: an open-source mesh processing tool. In: *Sixth Eurographics Italian Chapter Conference*. 2008:129–136.

25 Aursudkij B, McDowell GR, Collop AC. Cyclic loading of railway ballast under triaxial conditions and in a railway test facility. *Granul Matter*. 2009;11(6):391–401. https://doi.org/10.1007/s10035-009-0144-4.

26 En 13450 B. *Aggregates for Railway Ballast*. British Standards Institution; 2013.

27 de Bono J, McDowell GR. Micro mechanics of drained and undrained shearing of compacted and overconsolidated crushable sand. *Geotechnique*. 2018;68(7):575–589. https://doi.org/10.1680/jgeot.16.P.318.

28 de Bono J, McDowell GR. On the packing and crushing of granular materials. *Int J Solid Struct*. 2020;187:133–140. https://doi.org/10.1016/j.ijsolstr.2018.07.011.

29 de Bono J, McDowell GR, Wanatowski D. Discrete element modelling of a flexible membrane for triaxial testing of granular material at high pressures. *Géotech Lett*. 2012;2(4-6):199–203. https://doi.org/10.1680/geolett.12.00040.

30 Cil MB, Alshibli KA. 3D analysis of kinematic behavior of granular materials in triaxial testing using DEM with flexible membrane boundary. *Acta Geotech*. 2014;9 (2):287–298. https://doi.org/10.1007/s11440-013-0273-0.

31 Midi G. On dense granular flows. *Eur Phys J E*. 2004;14(4):341–365. https://doi.org/10.1140/epje/i2003-10153-0.

32 Christoffersen J, Mehrabadi MM, Nemat-Nasser S. A micromechanical description of granular material behavior. *J Appl Mech*. 1981;48(2):339. https://doi.org/10.1115/1.3157619.

33 Skinner AE. A note on the influence of interparticle friction on the shearing strength of a random assembly of spherical particles. *Geotechnique*. 1969;19(1):150–157.

34 Dai BB, Yang J, Zhou CY. Observed effects of interparticle friction and particle size on shear behavior of granular materials. *Int J GeoMech*. 2016;16(1), 04015011. https://doi.org/10.1061/(asce)gm.1943-5622.0000520.

35 Oger L, Savage SB, Corriveau D, Sayed M. Yield and deformation of an assembly of disks subjected to a deviatoric stress loading. *Mech Mater*. 1998;27(4):189–210. https://doi.org/10.1016/S0167-6636(97)00066-5.

36 Kruyt NP, Rothenburg L. Shear strength, dilatancy, energy and dissipation in quasi-static deformation of granular materials. *J Stat Mech Theor Exp*. 2006;7. https://doi.org/10.1088/1742-5468/2006/07/P07021.

37 Yang ZX, Yang J, Wang LZ. On the influence of inter-particle friction and dilatancy in granular materials: a numerical analysis. *Granul Matter*. 2012;14(3):433–447. https://doi.org/10.1007/s10035-012-0348-x.

38 Peña AA, Lizcano A, Alonso-Marroquin F, Herrmann HJ. Biaxial test simulations using a packing of polygonal particles. *Int J Numer Anal Methods GeoMech*. 2008;32 (2):143–160. https://doi.org/10.1002/nag.618.

39 Binaree T, Azéma E, Estrada N, Renouf M, Preechawuttipong I. Combined effects of contact friction and particle shape on strength properties and microstructure of sheared granular media. *Phys Rev E*. 2020;102(2), 22901. https://doi.org/10.1103/PhysRevE.102.022901.

40 Suiker ASJ, Fleck NA. Frictional collapse of granular assemblies. *J Appl Mech Trans ASME*. 2004;71(3):350–358. https://doi.org/10.1115/1.1753266.

41 Huang X, Hanley KJ, O`Sullivan C, Kwok CY. Exploring the influence of interparticle friction on critical state behaviour using DEM. *Int J Numer Anal Methods GeoMech*. 2014;38(12):1276–1297. https://doi.org/10.1002/nag.2259.

42 Thornton C. Numerical simulations of deviatoric shear deformation of granular media. *Geotechnique*. 2000;50(1):43–53. https://doi.org/10.1680/geot.2000.50.1.43.

43 Gong J, Zou J, Zhao L, Li L, Nie Z. New insights into the effect of interparticle friction on the critical state friction angle of granular materials. *Comput Geotech*. 2019;113 (March), 103105. https://doi.org/10.1016/j.compgeo.2019.103105.

44 Rowe PW. The stress-dilatancy relation for static equilibrium of an assembly of particles in contact. *Proc R Soc London Ser A Math Phys Sci*. 1962;269(1339):500–527. https://doi.org/10.1098/rspa.1962.0193.

45 Guo P, Su X. Shear strength, interparticle locking, and dilatancy of granular materials. *Can Geotech J*. 2007;44(5):579–591. https://doi.org/10.1139/T07-010.

46 Bolton MD. The strength and dilatancy of sands. *Geotechnique*. 1986;36(1):65–78. https://doi.org/10.1680/geot.1986.36.1.65.